INTERNATIONAL JOURNAL OF HYDROGEN ENERGY 37 (2012) 5735–5749

Available online at www.sciencedirect.com

SciVerse ScienceDirect

journal homepage: www.elsevier.com/locate/he

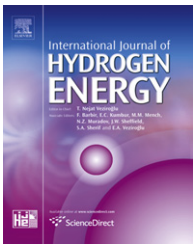

Experimental investigation and theoretical modeling of dehydriding process in high-pressure metal hydride hydrogen storage systems

Milan Visaria, Issam Mudawar*

Hydrogen Systems Laboratory (HSL) and Boiling and Two-Phase Flow Laboratory (BTPFL), Purdue University, West Lafayette IN 47907, USA

ARTICLE INFO

Article history:
Received 11 October 2011
Received in revised form
26 December 2011
Accepted 28 December 2011
Available online 28 January 2012

Keywords:
Hydrogen storage
Dehydriding
High-pressure metal hydride
Heat exchangers

ABSTRACT

This study explores the endothermic dehydriding (desorption) reaction that takes place in a high-pressure metal hydride (HPMH) hydrogen storage system when hydrogen gas is released to the fuel cell. The reaction is sustained by circulating warm fluid through a heat exchanger embedded in the HPMH powder. A systematic approach to modeling the dehydriding process is presented, which is validated against experimental data using two drastically different heat exchangers, one using a modular tube-fin design and the other a simpler coiled-tube design. Experiments were performed inside a 101.6-mm (4-in) diameter pressure vessel to investigate the influences of hydrogen release rate, heat exchanger fluid flow rate and fluid temperature on the dehydriding process for the HPMH $Ti_{1.1}CrMn$. It is shown the dehydriding reaction rate can be accelerated by increasing the fluid temperature and/or the rate of pressure drop. HPMH particles located in warmer locations close to heat exchanger surfaces both began and finished dehydriding earlier than particles farther away. 2-D and 3-D models were created in Fluent to assess the dehydriding performances of the modular tube-fin heat exchanger and coiled-tube heat exchanger, respectively. The models are shown to be quite accurate at predicting the spatial and temporal variations of metal hydride temperature during the dehydriding reaction.

1. Introduction

Environmental concerns and the rise in fossil fuel cost have created a need for alternative fuel solutions for a variety of mobile systems, especially automobiles. Hydrogen fuel cells constitute one such solution, but present a host of new technological challenges. Low density of hydrogen renders the task of storing a sufficient mass of hydrogen on-board a mobile system quite elusive. Different solutions have been proposed to tackle this problem, including storing the hydrogen in gas form at very high pressure, in liquid form at very low temperature, or in solid form by undergoing a chemical reaction in chemical hydrides, metal hydrides, or cryo-adsorbents [1–12]. The present study concerns storage in high-pressure metal hydrides (HPMHs), which offer higher volumetric storage capacity than most other storage options [10].

Use of HPMHs in hydrogen fuel cells relies on two reversible processes: hydriding and dehydriding [4]. Hydriding is associated with hydrogen absorption into the HPMH when the hydrogen is charged into the storage system at a filling station.

* *Corresponding author*. Tel.: +1 812 764 1910; fax: +1 765 494 0539.
E-mail address: mvisaria@purdue.edu (M. Visaria).

0360-3199/$ – see front matter
doi:10.1016/j.ijhydene.2011.12.140

Nomenclature

C_d	dehydriding rate constant, s^{-1}
c_p	specific heat
E_d	energy of dehydriding (desorption), J/mol-H_2
F	reaction progress, amount of hydrogen absorbed by metal hydride as a fraction of it maximum storage capacity
h	convective heat transfer coefficient
ΔH_d	enthalpy of dehydriding reaction (J/mol-H_2)
k	thermal conductivity
MW	molecular weight
P	pressure
P_{eq}	equilibrium pressure
P_o	atmospheric pressure
$\dot{q}'''$	volumetric heat generation rate, W/m^3
R	universal gas constant, 8.314 J/mol·K
R_{tc}	contact resistance, $mm^2 \cdot K/W$
r_1	inner radius of fluid tube
r_2	outer radius of fluid tube
ΔS_d	entropy of dehydriding reaction, J/mol-H_2 K
t	time
T	temperature
wt%	hydrogen to metal hydride mass ratio when completely hydrided

Greek Symbols

ρ	density

Subscripts

d	dedhydriding (desorption)
eff	effective
eq	equilibrium
fluid	heat exchanger fluid
H_2	hydrogen
i	internal
ic (i = 1–4)	thermocuple i in coiled-tube heat exchanger
im (i = 1,2)	thermocuple i in modular tube-fin heat exchanger
MH	metal hydride
ss	stainless steel.

This reaction is highly exothermic, releasing large amounts of heat. Dehydriding involves desorption of the hydrogen from the HPMH, an endothermic reaction that requires heat input to release the hydrogen to the fuel cell. Hence, a heat exchanger is essential to controlling both the hydriding and dehydriding reactions. In fact, the heat exchanger is the most crucial component of a HPMH storage system [10]. The present study is focused on the dehydriding reaction.

Several technical challenges must be overcome when designing a HPMH storage system. First, the system must meet the stringent weight and volume constraints of the mobile system. Second, the fueling must be achieved at the filling station within an acceptable duration. This means the heat produced from the ensuing hydriding reaction must be removed effectively by the heat exchanger and the reaction must reach near completion to ensure successful absorption of the hydrogen in the HPMH. Third, the storage system must be cold-start capable and release hydrogen gas to meet the fluctuating demands of the fuel cell even under harsh ambient conditions.

$Ti_{1.1}CrMn$ is one HPMH that has recently been recommended for on-board hydrogen storage. Despite its low gravimetric capacity (<2 wt% H_2), its volumetric capacity (>50 g H_2/l) is highest among all solid-state HPMH materials [10]. Another attribute of this material is that its maximum temperature during the hydriding reaction is only 85 °C, which is close to the operating temperature of the fuel cell. Previous studies have shown that a storage system using $Ti_{1.1}CrMn$ and an appropriately designed heat exchanger can achieve a hydrogen fill time (time needed at the filling station to complete 90% of the hydriding reaction) as low as 4 min 40 s [13]. $Ti_{1.1}CrMn$ has excellent cold-start capability as well. Unlike chemical hydrides and complex metal hydrides that require temperatures in excess of 120–220 °C to dehydride, HPMHs in general can dehydride and release the hydrogen at normal ambient temperatures. $Ti_{1.1}CrMn$ in particular can dehydride even at sub-zero temperatures.

Jemni and Nasrallah [14] developed a two-dimensional heat and mass transfer model for the dehydriding process in metal hydrides. They later performed dehydriding experiments using $LaNi_5$ as HPMH in a cylindrical vessel that was placed in a liquid bath [15]. They observed that the temperature of the liquid bath had a significant influence on desorption rate. At the end of 1800 s, the mass of hydrogen desorbed nearly doubled when the bath temperature was increased from 40 to 50 °C. Muthukumar et al. [16,17] performed numerical and experimental studies on storage systems using $MmNi_{4.6}Al_{0.4}$. They observed a drop in the hydride temperature when the dehydriding commenced, before warmer heat exchanger fluid caused the hydride temperature to rise. Mellouli et al. [18,19] performed experiments with a $LaNi_5$ storage system that was fitted with a spiral-tube heat exchanger. They developed a numerical model of the system that demonstrated the importance of the heat exchanger in reducing desorption time. Researchers employed different metal hydrides and heat exchanger designs to study and optimize both the hydriding and dehydriding processes [20–22]. Raju et al. [23,24] examined the feasibility of an on-board hydrogen storage system using sodium alanate. They developed system models simulating the process of hydriding and dehydriding process and performed drive cycle system simulations. Tange et al. [25] performed hydriding and dehydriding experiments on a metal hydride system, but for a very different application of load leveling of electricity in commercial buildings. However, the majority of heat exchanger studies centered on complex metal hydrides, which require relatively low pressures (below 50 bar) and high temperatures. The kinetics of these complex metal hydrides are quite different than those of HPMHs; the latter require pressures as high as 300–500 bar. In fact, no studies have been published on the heat transfer aspects of the dehydriding process in HPMHs. Addressing these aspects is precisely the goal of the present study.

In this study, experiments were performed to examine the desorption characteristics of $Ti_{1.1}CrMn$ and understand the

vital role of the heat exchanger in this process. Two very different prototype heat exchangers were tested to explore the influence of operating parameters on the dehydriding reaction, including hydrogen release rate, heat exchanger fluid flow rate, and fluid temperature. Computational models describing the dehydriding process were also developed, which serve the dual role of providing a detailed understanding of the temporal and spatial characteristics of the $Ti_{1.1}CrMn$ storage system and aiding in the optimization of heat exchanger design. The accuracy of these models is assessed by comparing predictions of key performance parameters against experimental data.

2. Experimental methods

This section describes the construction, assembly and experimental setup for each of the two prototype heat exchangers. This is followed by description of the operating procedure for each. It should be noted that both systems use containment vessels that are filled with activated $Ti_{1.1}CrMn$ powder and tested inside a 101.6-mm (4-in) diameter stainless steel pressure vessel.

2.1. *Modular tube-fin heat exchanger*

Fig. 1(a) shows a CAD rendering of the containment vessel employing the modular tube-fin heat exchanger. The heat exchanger itself consists of a network of aluminum fins extending from a central stainless steel U-tube. Dex-cool®, a commercial automotive antifreeze, flows through the U-tube to provide heating during the dehydriding process. The fins form pockets that maximize proximity to the metal hydride powder everywhere in the containment vessel. Stainless steel cover plates seal the hydride powder on both sides and contain fittings for the fluid tube, hydrogen inlet/outlet ports, and thermocouple feed-through. Each cover plate houses a porous stainless steel disk to prevent hydride powder from escaping the vessel as well as to diffuse the incoming hydrogen gas flow into all the pockets while capturing any impurities. Type-T thermocouples secured by hollow stainless steel tubes measure metal hydride temperatures at various locations. A hollow cylindrical sleeve (not shown in the figure) is slide over the cover plates to seal the entire containment assembly. The fluid tube and the fins occupy 29% of the pressure vessel internal volume, leaving the rest to be filled by the hydride powder. Since activated $Ti_{1.1}CrMn$ is highly reactive in the presence of air or moisture, the containment vessel is filled with the hydride powder inside a sealed glove box filled with argon gas. The 260-mm (10.25-in) long containment vessel is filled with 2.65 kg of $Ti_{1.1}CrMn$ powder with a packing density of 2.5 g/cc. Once the containment vessel is safely sealed and secured, it is transferred from the glove box to a secure test cell, where it is inserted inside the pressure vessel in preparation for the tests. Additional details concerning the construction of individual components of the containment vessel and heat exchanger, and description of the filling and assembly procedures, can be found in [26].

2.2. *Coiled-tube heat exchanger*

The coiled-tube heat exchanger consists of a coiled stainless steel tube that is embedded in the metal hydride powder inside a containment vessel. Fig. 1(b) shows a CAD rendering of the full containment vessel assembly. The fluid tube is coiled such that the inlet and outlet extend from the same side of the vessel. The coil is configured to maintain a distance from the hydride powder everywhere in the vessel no greater than 15 mm. Two stainless steel support tubes secure thermocouples in various locations in the hydride bed. The cover plates and containment vessel are similar in construction to those used with the modular tube-fin heat exchanger. The containment vessel is 335-mm (14-in) long and stores 4.0 kg of $Ti_{1.1}CrMn$ powder, packed with a density of 2.2 g/cc. In the absence of fins, the coiled-tube heat exchanger occupies a mere 7% of the containment vessel volume. Additional details of the construction and assembly of this system are available in [27,28].

2.3. *Experimental procedure*

The testing procedure involves securing the assembled and sealed containment vessel inside the pressure vessel. The heat exchanger is first connected to the hydrogen and fluid lines, and various sensors are connected to an external instrumentation panel for remote monitoring and recording of data. The fluid tube is connected to a chiller capable of delivering 20 lpm of heat exchanger fluid at temperatures between 0 and 35 °C. Hydrogen lines are then connected to the pressure vessel. The source of hydrogen is a number of pressure cylinders containing 5.0-grade hydrogen gas at 410 bar (6000 psi). Flow meters measure the flow rate of hydrogen gas entering and leaving the pressure vessel. Pressure sensors measure the pressure within the pressure vessel and at various external locations. Fluid flow rate as well as temperature and pressure are measured at the vessel's inlet and outlet. Temperatures of the metal hydride powder at various locations within the vessel are continuously monitored and recorded. Pressure regulators are used to control the rate of hydrogen gas supply to, and exit from the pressure vessel. On/off valves allow the supply and vent sides of the pressure vessel to be isolated from one another.

Before starting the dehydriding experiments, the metal hydride has to be in fully hydrided state. This is achieved by opening the supply side on/off valve to introduce the hydrogen gas at a controlled rate. The pressure in the vessel is increased to 280 bar in 60 s. The supply side on/off valve is kept open and the pressure maintained at 280 bar until hydriding reaction is complete. All this while, the vent side on/off valve remains closed. The exothermic hydriding reaction causes the metal hydride temperature to increase to a maximum of 50 °C. The released heat is removed by the heat exchanger fluid supplied between 0 and 20 °C. Completion of the hydriding reaction is evidenced by both a sharp drop in metal hydride temperature (indicating a cessation of heat generation) and a drop in the hydrogen flow rate to zero. Once the metal hydride is completely hydrided, the supply side on/off valve is closed and the system is ready for the dehydriding experiments.

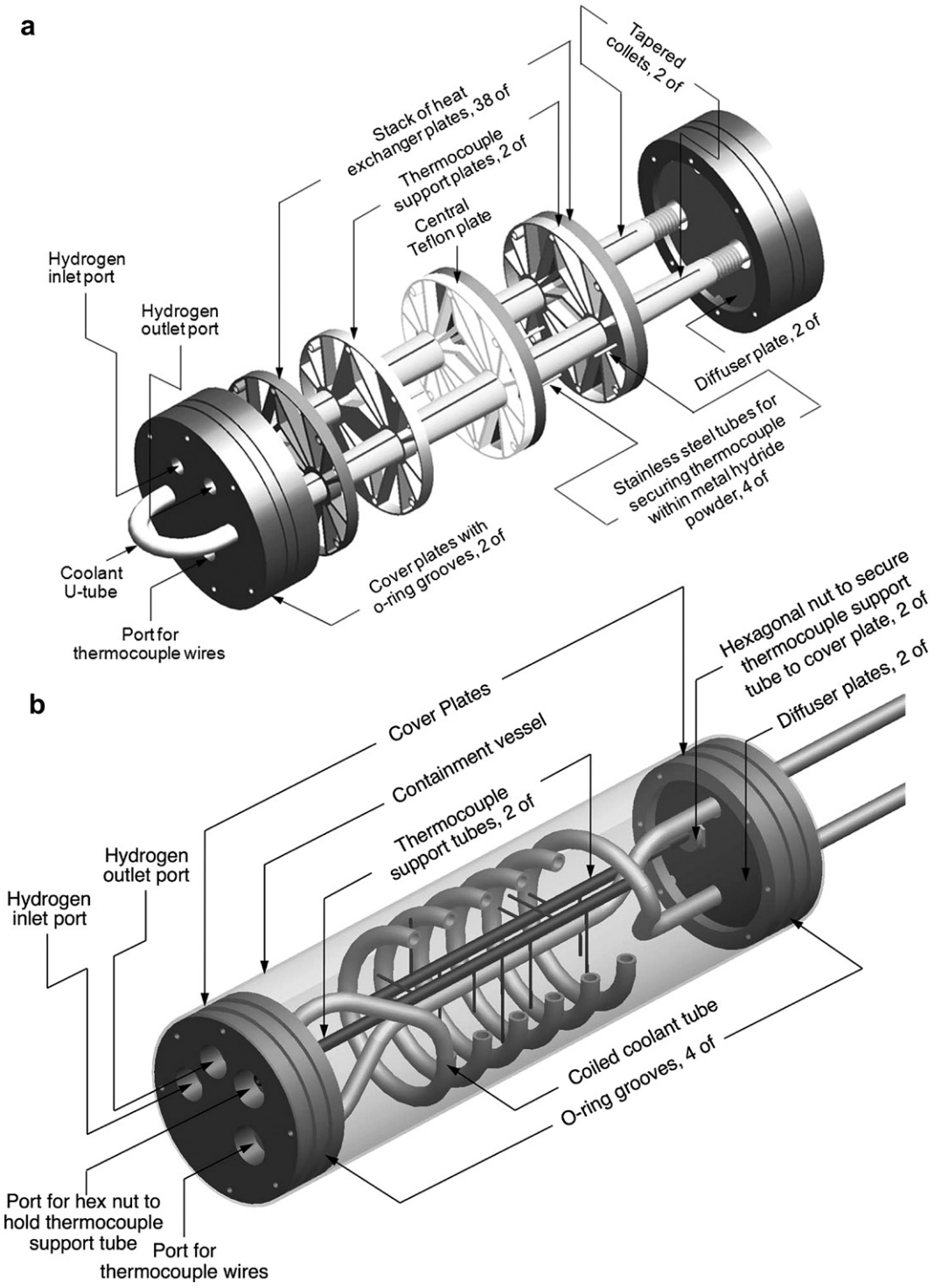

Fig. 1 – Detailed 3-D renderings of containment vessels utilizing (a) modular tube-fin heat exchanger and (b) Coiled-tube heat exchanger.

In contrast to hydriding, dehydriding is an endothermic reaction, achieved by reducing the pressure and supplying heat to the hydride powder. At the end of the hydriding experiment, when the pressure in the vessel is at 280 bar, the vent side on/off valve is opened to release the hydrogen gas. The rate of hydrogen gas exiting the vessel is controlled by the pressure regulator. Due to hysteresis (explained later), dehydriding does not begin once the pressure is reduced. When the vent side on/off valve is opened, hydrogen gas stored in the empty spaces of the vessel and interstitial gaps of the metal hydride powder is released. But the dehydriding reaction commences only when the pressure drops below the

temperature-dependent dehydriding equilibrium pressure (discussed later). Generally, the dehydriding reaction can be accelerated by supplying the fluid at warmer temperature of 20–30 °C. Dehydriding is deemed complete when the temperature of the hydride powder becomes uniform with no hydrogen outflow detected. Thereafter, the pressure vessel is isolated from the hydrogen and fluid lines and maintained at a positive pressure of 7 bar until the next test.

3. Experimental results

A total of six tests, three for each heat exchanger, were performed for different hydrogen release rates, fluid temperatures and flow rates, and ambient temperatures; the latter was not controlled during the experiments. Table 1 provides a summary of operating conditions for these tests. Temperatures measured by two thermocouples in the tube-fin heat exchanger and four thermocouples in the coiled-tube heat exchanger are used in presenting the performance results. Located at varying distances from the heat exchanger surface, these thermocouples capture spatial variations of the metal hydride temperature response inside the storage vessel. Table 2 shows the distances of thermocouples from the nearest heat exchanger surface (fin for the modular tube-fin heat exchanger and bare tube for the coiled-tube heat exchanger).

To start the dehydriding process, the vessel is depressurized gradually from its peak hydriding pressure of 280 bar by releasing hydrogen from the vessel. But the dehydriding reaction does not begin until the pressure falls below the hydride's equilibrium pressure (100 bar for a metal hydride at 20 °C, and decreasing with decreasing temperature). Depressurization can be divided into two regions. The first spans the time needed for the pressure to drop from peak hydriding pressure to the equilibrium pressure, during which no dehydriding reaction can occur, and only hydrogen gas stored in the vessel gaps or between hydride particles is released. The second is the region below the equilibrium pressure, where the dehydriding reaction takes effect. In this second region, hydrogen gas that had chemically bonded with the metal hydride is released by the endothermic dehydriding reaction. A sharp drop in the hydride temperature marks the initiation of the dehydriding reaction because of the large amounts of heat absorbed. Since the focus of this study is the dehydriding reaction, experimental results corresponding to only the second region below the equilibrium pressure are presented and discussed.

3.1. Modular tube-fin heat exchanger results

Shown in Fig. 2(a) and (b) are data from experiments performed with the modular heat exchanger during tests 1M and 2M, respectively. Shown in these figures are profiles of vessel pressure, hydrogen release rate, and temperatures of metal hydride and heat exchanger fluid. Hydride powder temperature was measured at two locations, T1m and T2m. T1m is located in a smaller powder pocket close to the heat exchanger surface, while T2m is located in the center of the largest pocket. The fluid temperature is the average of the measured inlet and outlet temperatures. During the dehydriding reaction, differences between the fluid inlet and outlet temperatures were less than 1 °C.

During test 1M, the fluid was maintained at 25 °C and the pressure regulator set for a maximum hydrogen release rate of 0.3 g/s, causing the pressure to drop from 65.7 to 29.0 bar in 2 min. The dehydriding reaction caused the hydride temperature to drop from 5 to −12.4 °C in the first 2 min of the reaction. At the end of 2 min, the hydrogen release rate started to drop because the rate of dehydriding could not keep up with the set release rate of 0.3 g/s. There are two main reasons for the reduction in dehydriding rate: (a) low hydride temperatures reduced the equilibrium pressure significantly, thereby reducing the driving potential for the reaction, and (b) metal hydride particles neared completion of the dehydriding reaction. At 2.6 min, when the hydrogen release rate had fallen to 0.22 g/s, the pressure regulator was reset to a new maximum flow rate of 0.1 g/s for a period of 0.6 min. During the period from 2.6 to 3.2 min, cooling rate slowed considerably, evidenced by the change in slope of the temperature plot, due to the reduction in the rate of pressure drop. At 3.2 min, the maximum hydrogen release rate was reset to 0.3 g/s. This caused the hydrogen outflow rate to jump to 0.2 g/s and then gradually slow to 0.07 g/s at 5.3 min, at which point the vent side on/off valve was closed. At 5.3 min, the pressure reached 7 bar, the lowest pressure at which the vessel was maintained. At this time, thermocouple T2m measured the lowest temperature for the test of −40 °C, which is the equilibrium temperature corresponding to 7 bar. Notice that the lowest temperature measured by thermocouple T1m is −23 °C, which was reached at an earlier time of 3.8 min. These differences can be explained by the location of T1m in a smaller pocket and closer to fins, where the hydride powder had a superior heat transfer rate and could complete dehydriding faster than at T2m. By the end of 5.3 min, most of the metal hydride had dehydrided and the vent valve was

Table 1 – Summary of operating conditions for experiments performed.

	Test no.	H_2 release rate (g/s)	Fluid flow rate lpm (gpm)	Fluid Temp. (°C)	Ambient Temp. (°C)
Modular	1M	0.30–0.08	12.5 (3.3)	25.0	−9.0
	2M	0.15–0.08	17.5 (4.6)	23.2–26.2	5.0
	3M	0.22–0.08	17.5 (4.6)	20.0	−2.0
Coiled-tube	1C	0.13	13.0 (3.4)	1.5–12.0	7.0
	2C	0.14	15.2 (4.0)	17.0–32.0	12.0
	3C	0.17	14.8 (3.9)	27.0	9.0

Table 2 – Placement of thermocouples used to measure metal hydride temperature.

Thermocouple no.	Minimum distance from fluid tube surface (mm)
Modular	
1m	2.5
2m	8.4
Coiled-tube	
1c	4.3
2c	8.4
3c	11.5
4c	13.0

closed. The warm fluid continued to heat the hydride, and the remaining small amount of hydrogen absorbed by the hydride was released into the pressure vessel. This is manifest by the slight increase in pressure from 7 to 9 bar at the end of 9 min. At 9 min, the vent side on/off valve was briefly opened and then closed to expel the residual hydrogen gas from the vessel. The hydride temperatures continued to rise and the experiment was concluded when the hydride temperature became uniform.

In test 2M, the maximum hydrogen release rate was set to 0.15 g/s. The fluid temperature rose linearly from 23.3 to 26.2 °C in the first 4 min and was maintained at 26.2 °C for the remainder of the test. The dehydriding reaction commenced at a hydride temperature of 10 °C, and the temperature began to decrease as the reaction progressed. Thermocouple T1m measured its minimum temperature of −11.7 °C at 6.1 min, while the lowest temperature measured by T2m was −36.8 °C, which was reached at 8.3 min. The hydride temperatures during the dehydriding reaction in test 2M are slightly higher than in test 1M because of the slower hydrogen release rate for test 2M. At 7.2 min, the pressure reached 14 bar, at which point most of the hydride had completed dehydrided. At 7.2 min, the hydrogen outflow rate began to drop considerably because dehydriding rate could not keep up with the set outflow rate of 0.15 g/s. At 8.3 min, when the pressure reached 7.7 bar and dehydriding was complete, the vent side on/off valve was closed to isolate the pressure vessel. The fluid flow was stopped and the test concluded once the hydride temperature became uniform.

3.2. *Coiled-tube heat exchanger results*

Fig. 3(a) and (b) show data from tests 1C and 2C, which were performed with the coiled-tube heat exchanger. Temperatures were measured at four locations, T1c to T4c, as indicated in the inset in each figure. These locations correspond to increasing distances from the fluid tube, T1c being the closest and T4c the farthest. The locations are chosen to help understand the spatial variations of hydride temperature and the influence of distance from the cooling surface on the dehydriding reaction.

In test 1C, maximum hydrogen outflow rate was set at 0.13 g/s. The fluid temperature was around 2 °C for the first 20 min and then increased fairly linearly to 9 °C in the next 10 min. Notice that, in test 1C, dehydriding did not begin until

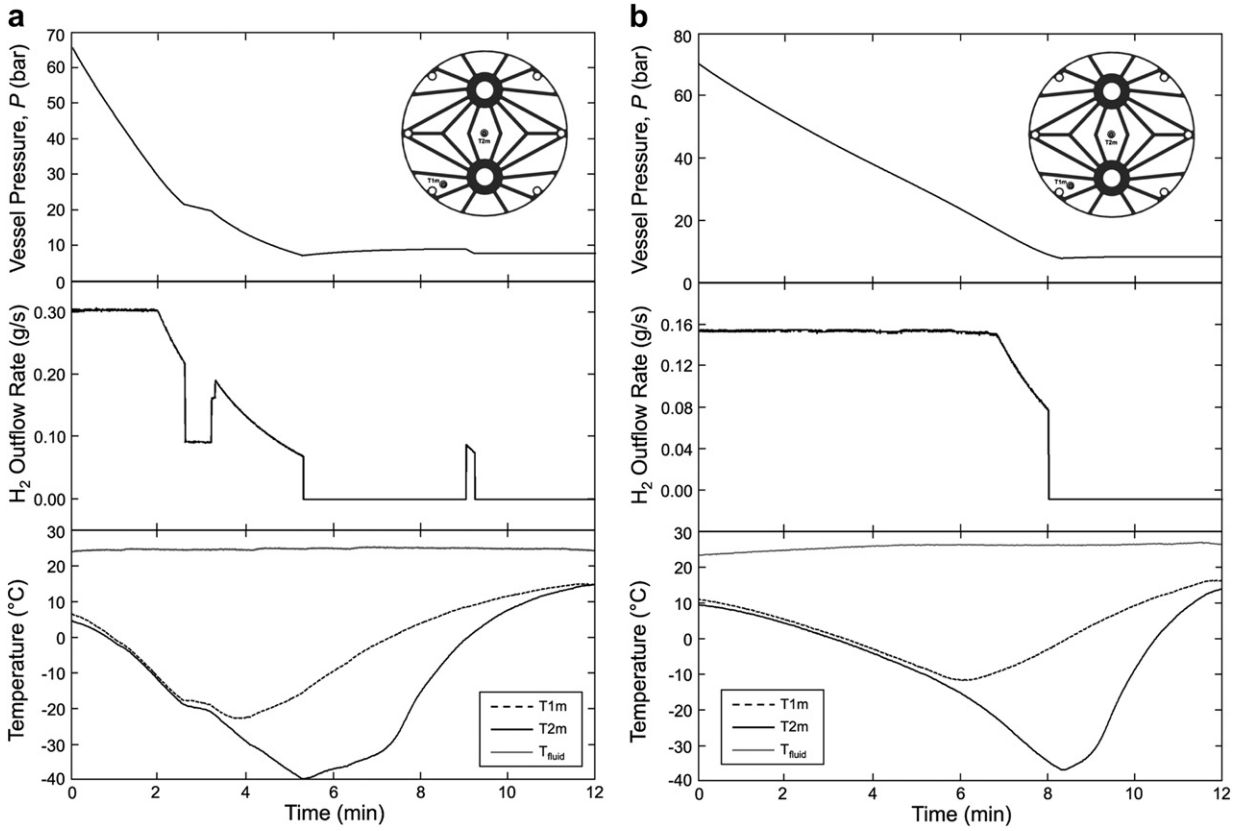

Fig. 2 – Experimental dehydriding data for modular tube-fin heat exchanger from (a) test 1M and (b) test 2M.

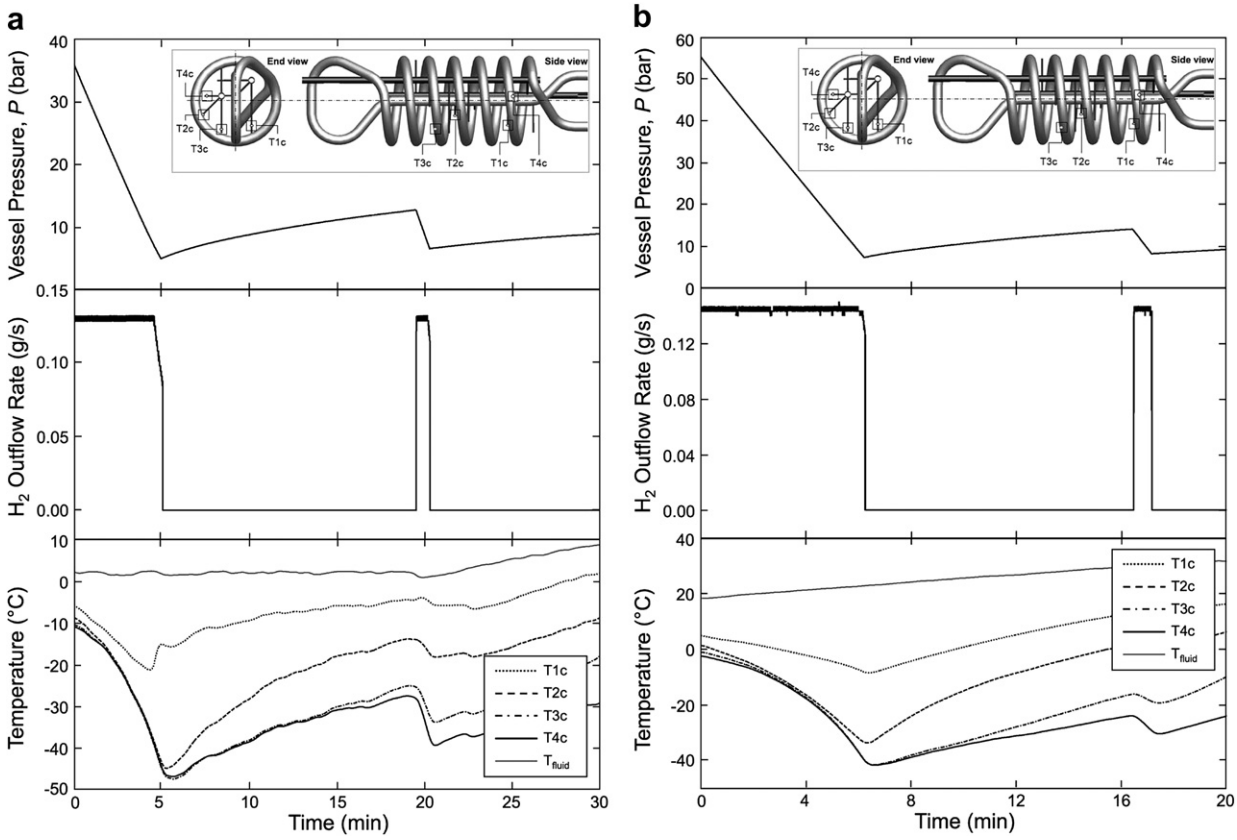

Fig. 3 – Experimental dehydriding data for coiled-tube heat exchanger from (a) test 1C and (b) test 2C.

the pressure reached 35 bar, which is lower that the 65–70 bar pressure corresponding to the initiation of dehydriding in tests 1M and 2M. The reason for the lower pressure in test 1C is low metal hydride temperature. In test 1C, the hydride was around −10 °C, at which the dehydriding equilibrium pressure is lower that in tests 1M and 2M. The 0.13 g/s hydrogen release rate caused the pressure in test 1C to drop from 36 to 5 bar in 5 min, and the metal hydride to cool to a minimum temperature of −47.2 °C corresponding to an equilibrium pressure of 5 bar, which was measured by thermocouples T3c and T4c at 5.5 min. With thermocouple T1c located closest to the fluid tube, T1c measured a lowest temperature of −21.4 °C, significantly higher than the minimum for T3c and Tc4, which was reached earlier as well, at 4.3 min. This is evidence of the metal hydride particles at T1c finishing dehydriding earlier than particles at the other locations. At the end of 5 min, the vent side on/off valve was closed. The metal hydride temperature began to rise because of heating from the warmer fluid. The dehydriding reaction continued and the pressure rose as the gas accumulated in the vessel. At 19.5 min, the pressure reached 12.7 bar, at which point the supply valve was closed. The vent side on/off valve was opened for a short duration, as indicated by the spike in hydrogen outflow rate, to remove residual hydrogen gas from the vessel, before being closed. During the time the vent-side valve was opened, the pressure dropped from 12.7 to 6.5 bar, causing the metal hydride to dehydride further, and the metal hydride temperature to fall once more. The highest temperature drop of 12 °C during this renewed dehydriding was measured by thermocouple T4c. Finally, when the hydrogen gas was released from the vessel and pressure reached 7 bar, the on/off valve was closed. However, the pressure continued to rise, albeit slowly, proving the metal hydride had not completely dehydrided, and the hydrogen continued to be released in small amounts.

In test 2C, the hydrogen outflow rate was set to 0.143 g/s and the fluid temperature increased fairly linearly from 18.3 to 32 °C for the duration of the test. Dehydriding started when the metal hydride was around 0 °C and the vessel pressure at 55 bar. As the dehydriding progressed, both the pressure and metal hydride temperature decreased. The vent valve was closed when the vessel reached 7 bar. The metal hydride temperatures measured in test 2C during the dehydriding reaction were higher that those in test 1C because of the higher fluid temperature in test 2C. The lowest temperature for test 2C of −41.6 °C was measured by thermocouples T3c and T4c. T1c and T2c measured higher lowest temperatures of −8.5 and −33.6 °C, respectively. At 6.2 min, the vent valve was closed and both the hydride temperature and vessel pressure began to rise. As the dehydriding continued, hydrogen gas accumulated in the vessel and the pressure rose to 14 bar. At 16.4 min, the vent side on/off valve was opened to release the hydrogen gas from the vessel and then closed once again before the test was concluded.

4. Computational models

Computational models were developed to predict the dehydriding reaction for both the modular tube-fin heat exchanger and coiled-tube heat exchanger. These predictions will be compared to experimental data in the next section. This section will describe the governing equations, properties of the metal hydride used in the models, and the computational domains adopted for the two heat exchanger designs.

4.1. Equilibrium pressure

The hydriding and dehydriding processes for metal hydrides are dictated by the equilibrium pressure. At a given hydride temperature, hydriding will occur only when the pressure is above equilibrium. Conversely, dehydriding will occur only when the pressure is below equilibrium. However, equilibrium pressure is different for the hydriding and dehydriding reactions as shown in Fig. 4 for $Ti_{1.1}CrMn$. The equilibrium pressure for each is a function of the metal hydride temperature and depends on two metal hydride kinetic properties, enthalpy of reaction and entropy of reaction. Both equilibrium pressures increase with increasing temperature and, within the temperature range of the present study, the hydriding equilibrium pressure is greater than the dehydriding equilibrium pressure. For example, at 10 °C, hydriding will start when the vessel pressure exceeds 130 bar. However, for dehydriding to take place at the same temperature, the pressure must be set below 70 bar. The equilibrium pressures for the two reactions are predicted by the van't Hoff equation [10]. The same equation is used to predict both equilibrium pressures, the difference comes from differences in the values of enthalpy of reaction and entropy of reaction for the two processes. Equilibrium pressure for the dehydriding reaction is given by [10]

$$P_{eq,d} = P_o \exp\left(\frac{\Delta H_d}{RT} - \frac{\Delta S_d}{R}\right), \tag{1}$$

where P_o, ΔH_d, ΔS_d and R are atmospheric pressure, enthalpy of reaction, entropy of reaction for desorption, and universal gas constant, respectively. The greater the difference between the equilibrium and vessel pressures, the greater is the driving potential for the reaction.

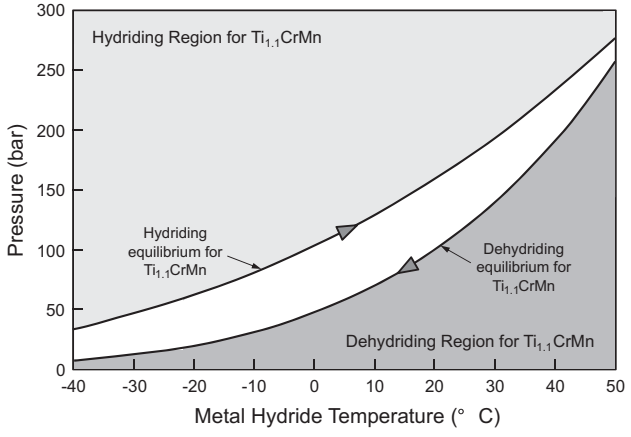

Fig. 4 – Variation of equilibrium pressure with temperature during hydriding and dehydriding of $Ti_{1.1}CrMn$.

4.2. Governing equations

Using a modified form of an equation derived in [29,30], the rate of dehydriding is given by

$$\frac{dF}{dt} = C_d \exp\left(\frac{-E_d}{RT}\right) \ln\left(\frac{P}{P_{eq,d}}\right) F, \tag{2}$$

where C_d and E_d are the dehydriding rate constant and activation energy for desorption, respectively. The parameter F is the amount of hydrogen absorbed (stored) in the metal hydride as a fraction of its total capacity. $F = 1$ when the hydride is in a completely hydrided state, and $F = 0$ when the dehydriding reaction is complete. Because the vessel pressure, P, is always lower than the dehydriding equilibrium pressure, $P_{eq,d}$, during the dehydriding reaction, dF/dt is negative for dehydriding.

As a result of the endothermic dehydriding reaction, heat is absorbed by the metal hydride at a rate that is given by [10]

$$\dot{q}''' = \frac{dF}{dt} \frac{(wt\%)\rho_{MH}}{MW_{H_2}} \Delta H_d, \tag{3}$$

where wt%, MW_{H_2}, and ρ_{MH} are the maximum hydrogen storage capacity of the hydride, molecular weight of hydrogen, and packing density of the hydride powder, respectively.

Equations (1)–(3) show that a higher hydride temperature leads to both higher equilibrium pressure and faster dehydriding rate. However, a faster reaction rate in turn increases heat absorption rate, which causes the metal hydride temperature to fall. This slows the rate of reaction unless sufficient heat is provided to the metal hydride. This demonstrates the interdependence of the three equations on one another, and highlights the importance of the heat exchanger at achieving and maintaining quick dehydriding rates.

In this study, Eqs. (1)–(3) are applied to the computation model and solved simultaneously along with a 2-D transient heat diffusion equation for the modular fin-tube heat exchanger, and a 3-D equation for the coiled-tube heat exchanger.

4.3. Metal hydride properties

Listed in Table 3 are the properties of $Ti_{1.1}CrMn$ used in the models. Because studies on this material are quite sparse, and it is difficult measuring the properties at high pressures, some of the properties are obtained from measurements with other metal hydrides. The value of activation energy for desorption of $Ti_{1.1}CrMn$ of $E_d = 16{,}500$ J/mol-H_2 is based on measurements by Suda et al. [30] for the metal hydride $LaNi_5$. $Ti_{1.1}CrMn$ has better dehydriding kinetics than hydriding kinetics. The measured reaction rate for desorption is $C_d = 300\ s^{-1}$, twice the rate for absorption. It must be noted that the hydriding and dehydriding reactions are quite insensitive to the reaction rate constants as shown in [10] for the absorption reaction. Experiments were performed at the Purdue University Hydrogen Systems Laboratory to measure some of the

Table 3 – Metal hydride properties used in models.

Kinetic properties		Source
Activation energy:	$E_d = 16.5$ kJ/mol of H_2	[20,27]
Reaction rate:	$C_d = 300\ s^{-1}$	Measured
Enthalpy of desorption:	$\Delta H_d = -24500$ J/mole of H_2	Measured [27,28]
Entropy of desorption:	$\Delta S_d = -122$ J/mole of H_2	Measured [27,28]
H_2 storage capacity:	1.5 wt% (Modular)	Measured
	1.3 wt% (Coiled-tube)	Measured
Thermal Properties		
Packing density:	$\rho_{MH} = 2.50$ g/cc (Modular)	Measured
	$\rho_{MH} = 2.22$ g/cc (Coiled-tube)	Measured
Effective thermal conductivity:	$k_{MH} = 0.75$ W/m K	[24,25]
Specific heat:	$c_{p,MH} = 750$ J/kg K	[24,25]
Contact resistance:	$R_{tc} = 1000\ mm^2 \cdot K/W$	[24,25]

properties of $Ti_{1.1}CrMn$. The measured values of enthalpy and entropy of dehydriding reaction were $\Delta H_d = -24{,}500$ J/mol-H_2 and $\Delta S_d = -122$ J/mol-$H_2 \cdot K$, respectively. These values are consistent with those measured by Suda et al. [30] and Voskuilen et al. [31] for $Ti_{1.1}CrMn$. The hydrogen storage capacity was measured using the Sievert apparatus [31]. Different batches of activated $Ti_{1.1}CrMn$ were used to test the two different heat exchangers. The batch used to test the modular tube-fin heat exchanger had a maximum hydrogen storage capacity of 1.5 wt%, while the batch in the coiled-tube heat exchanger had a capacity of 1.3 wt%. In the modular tube-fin heat exchanger tests, the metal hydride powder was packed with an average density of 2.5 g/cc compared to 2.22 g/cc for the coiled-tube heat exchanger.

The thermal properties of $Ti_{1.1}CrMn$ were measured at high pressures using the Transient Plane Source (TPS) method [32]. Although the thermal properties vary with pressure, temperature and hydrogen content, constant properties are used in the models. They include an effective thermal conductivity of $k_{MH} = 0.75$ W/m·K and specific heat of $c_{p,\ MH} = 750$ J/kg·K. A detailed explanation and justification for using these values can be found in [28]. Using the TPS system, contact resistance, R_{tc} was determined to range from 400 to 2000 $mm^2 \cdot K/W$. The contact resistance decreased with increases in pressure and/or hydrogen content. For the greater part of the dehydriding reaction in the present experiments, contact resistance should be on the lower side because hydrogen absorption by the metal hydride causes the hydride to expand against the heat exchanger and containment vessel walls. Therefore, a constant contact resistance of $R_{tc} = 1000\ mm^2 \cdot K/W$ is assumed in the models.

4.4. *Computational domain of modular fin-tube heat exchanger*

Fig. 5(a) shows the computational domain for the model constructed for the modular tube-fin heat exchanger. During the experiments, the difference between fluid temperatures at the inlet and the outlet was less than 1 °C, producing a fairly 2-D temperature distribution in the heat exchanger's cross-section. This, along with geometrical symmetry, facilitates using a 2-D model of only one-fourth the cross-section to explore the heat exchanger's performance.

The model requires assigning initial conditions for the vessel pressure and metal hydride temperature. The initial pressure is set equal to the pressure measured at the onset of

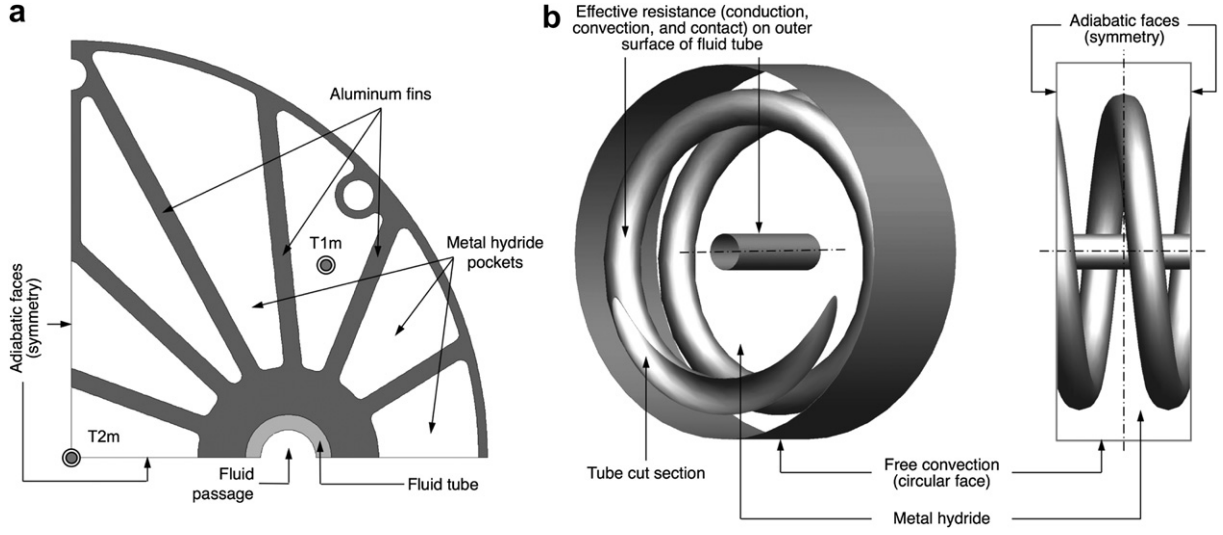

Fig. 5 – Computation domains of (a) 2-D modular fin-tube heat exchanger model and (b) 3-D coiled-tube heat exchanger model.

the dehydriding reaction. This is the pressure at which the slope of the hydride temperature profile changes sharply. The vessel pressure profile measured during the experiments is input to the model. Initial hydride temperature is set equal to the average of hydride temperature measured at the onset of the dehydriding reaction. It is further assumed that the metal hydride is initially in a completely hydrided state ($F = 1$).

Boundary conditions are applied along the inner wall of the fluid tube, interfaces between the hydride powder and fins, and outer circumference. The vertical and horizontal boundaries of the computational domain are assumed adiabatic due to symmetry in the heat exchanger's cross-section. Free convection is assumed along the circumference. Knowing the ambient conditions, the free convection heat transfer coefficient is determined form a correlation appropriate to the heat exchanger's outer geometry. Contact resistance is assumed along the interface between the metal hydride and aluminum fins. For the inner wall of the fluid passage, a convective heat transfer coefficient is determined from a correlation for turbulent internal flow based on the measured fluid flow rate. The convective boundary condition includes both the convective coefficient and measured fluid temperature.

4.5. *Computational domain of coiled-tube heat exchanger*

Shown in Fig. 5(a) is the computational domain for the coiled-tube heat exchanger model. Coil symmetry facilitates modeling only a small section of the vessel. The width of the domain is one and a half times the coil pitch. Although symmetry permits modeling only half a coil pitch, a wider computational allows more thermocouple locations to be precisely reproduced in the model. To simplify the model and meshing process, the fluid tube is modeled as a hollow tube, and an equivalent resistance applied to the tube surface.

The initial conditions for the coiled-tube heat exchanger model are identical to those of the modular tube-fun heat exchanger.

Boundary conditions are applied along the two faces of the computational domain, fluid tube wall and outer circumference of the vessel. The front and back faces of the domain are assumed adiabatic due to symmetry. Conduction and free convection are assumed along the outer circumference. An effective heat transfer coefficient and measured fluid temperature are used to model the fluid tube boundary. The effective heat transfer coefficient, h_{eff}, accounts for contact resistance between the metal hydride and outer surface of the

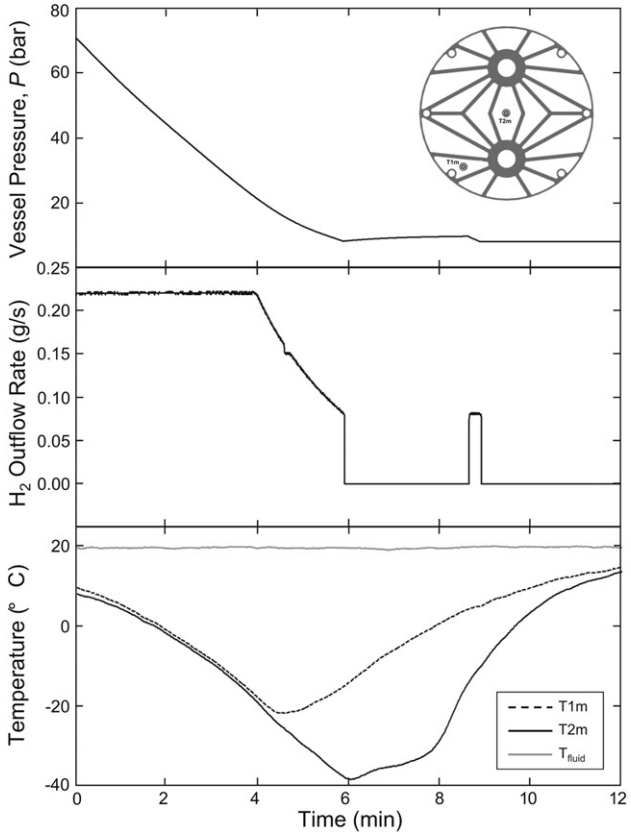

Fig. 6 – Experimental dehydriding data for modular fin-tube heat exchanger from test 3M.

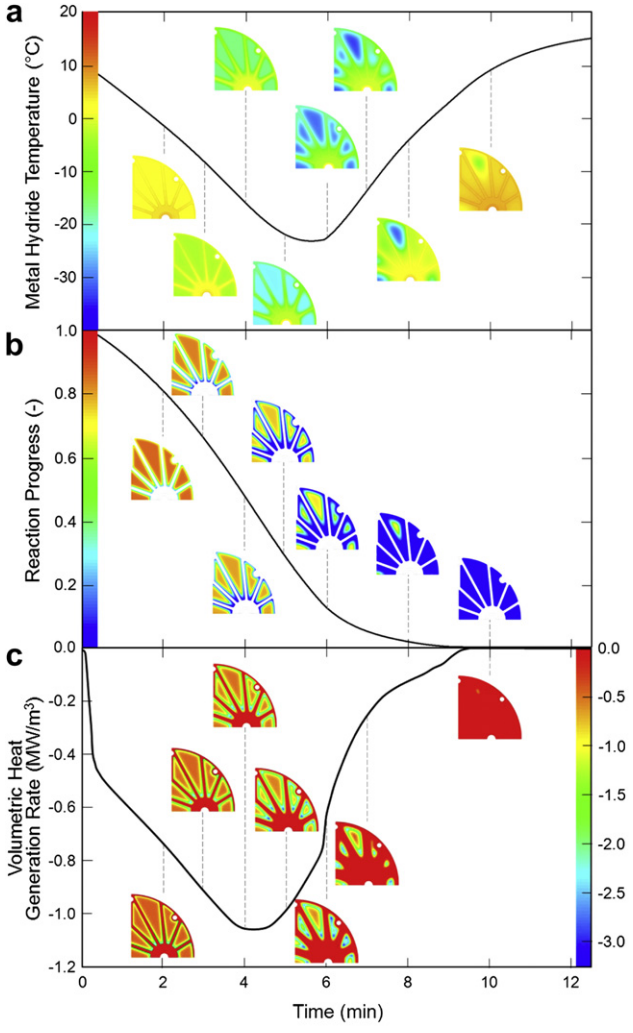

Fig. 7 – Temporal variations of spatial averages and spatial contour plots of (a) Metal hydride temperature, (b) Reaction progress, and (c) volumetric heat generation rate during dehydriding under operating conditions of test 3M.

fluid tube, conduction resistance across the tube wall, and convection inside the tube.

$$\frac{1}{h_{eff}} = \frac{r_2}{r_1}\frac{1}{h_i} + \frac{r_2}{k_{ss}}\ln\left(\frac{r_2}{r_1}\right) + R_{tc}, \quad (4)$$

where h_i, k_{ss}, r_1 and r_2 are the internal convective coefficient, thermal conductivity of stainless steel, inner radius of the tube, and outer radius, respectively.

5. Results of computational models

5.1. Contour plots

The computational models constitute powerful tools for understanding the detailed spatial distributions of key performance parameters of the two heat exchanger designs, a task that cannot be accomplished experimentally. In this section, representative transient spatial contour plots of temperature, reaction progress and volumetric heat rate during the dehydriding reaction are presented for both heat exchangers.

5.1.1. Experimental results and predictions for modular fin-tube heat exchanger

Fig. 6 shows temporal profiles of pressure, hydrogen outflow rate and metal hydride and fluid temperatures measured during test 3M. The maximum hydrogen outflow rate in this test was set to 0.22 g/s and the fluid temperature to 20 °C. At about 4 min, a drop in the hydrogen outflow rate is observed as the dehydriding rate fell short of matching the set outflow rate. Just before 6 min, the vent side on/off valve was closed. At 8.3 min, the valve was opened and closed shortly thereafter (manifest by the spike in the outflow rate plot) to release any residual hydrogen gas, before the test was concluded.

Spatial contour plots were computed for the operating conditions of test 3M. Fig. 7(a) shows the contours of temperature distribution plotted along with the temporal profile of average metal hydride temperature. Initially, the metal hydride is at a uniform temperature of 10 °C and the fluid at 20 °C. The metal hydride cools as the hydriding reaction progresses. As the hydrogen gas is released, the pressure begins to drop. This pressure drop, along with the heating provided by the fluid, allows the dehydriding reaction to continue. During the first 4 min, metal hydride temperatures are uniform irrespective of location. Thereafter, the temperature of metal hydride particles close to the fins begins to rise because of the warmer fluid, while particles away from fins

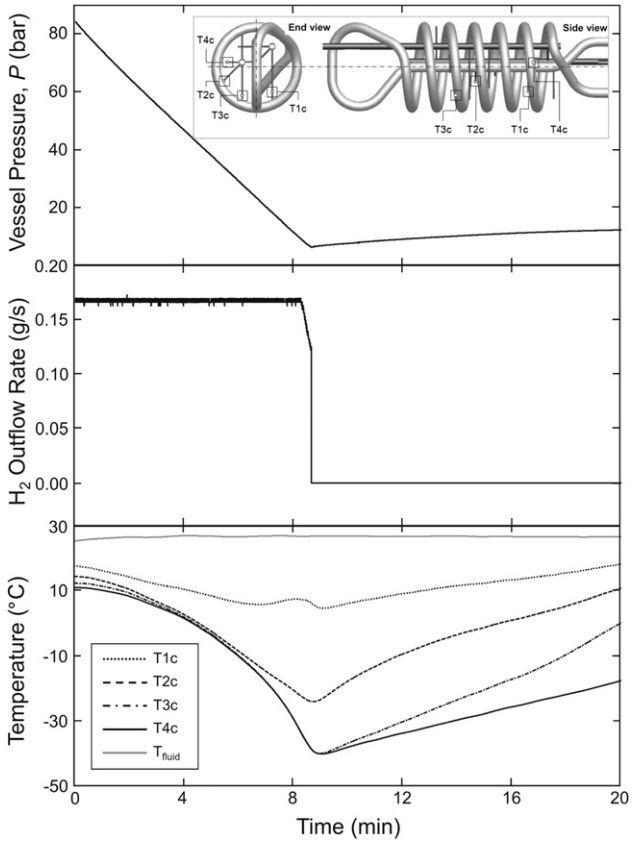

Fig. 8 – Experimental dehydriding data for coiled-tube heat exchanger from test 3C.

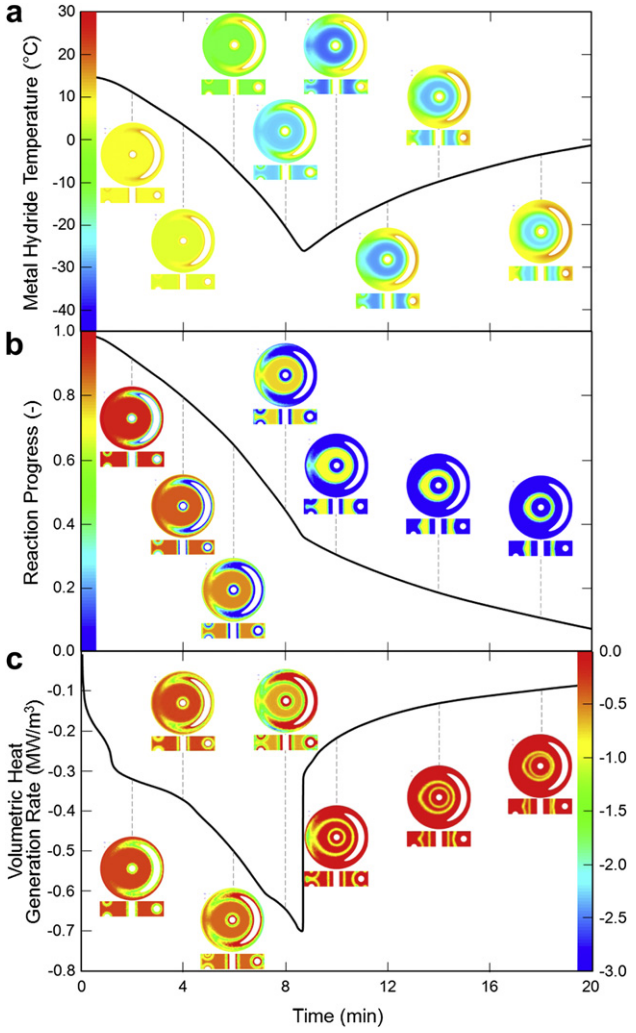

Fig. 9 – Temporal variations of spatial averages and spatial contour plots of (a) Metal hydride temperature, (b) Reaction progress, and (c) volumetric heat generation rate during dehydriding under operating conditions of test 3C.

continue to cool by the hydriding process. The dehydriding reaction progresses from the fins to locations farther away. The average hydride temperature is lowest at 5.8 min, after which it starts to rise. However, the temperature of metal hydride particles in the larger pocket continues to drop further because of delayed dehydriding reaction. In fact, the center of the largest pocket reaches a lowest temperature of −40 °C, significantly below that minimum average temperature.

Fig. 7(b) shows the variation of average reaction progress with time along with spatial contour plots of the reaction progress. Initially, the reaction is initiated along the fin surfaces close to the fluid tube, and hydride particles located in the inner corners of pockets close to the fluid tube finish reaction reacting ($F = 0$) within the first 3 min. The reaction then proceeds toward the centers of the pockets. The slope of the curve changes at 4 min when the reaction is over 50% complete, indicating a decrease in reaction rate. At 5 min, metal hydride particles along the fin surfaces are completely dehydrided, while particles located in the middle of the pockets are only 70% dehydrided. At 6.3 min, 90% of the average reaction is complete and the reaction rate drops significantly. However, because of the delayed reaction in the middle of the pockets, it takes an additional 2.7 min for all the powder to become 90% dehydrided.

Fig. 7(c) shows the average volumetric heat generation rate along with spatial contour plots for the heat generation rate. Note that the vertical axis to the left provides the scale for the average plot, while the axis to the right is for the contour plots. The heat rate is negative because the heat is being absorbed by the metal hydride. The highest magnitude of heat rate occurs at 4 min, which is also where the reaction rate is highest. After 4 min, the magnitude of heat rate decreases. This matches well with the experimental results, which showed the hydrogen outflow rate dropping after 4 min. Notice that, because of spatial variations in the dehydriding reaction, local heat rates as large as −3.25 MW/m^3 are achieved when the peak value for the average heat rate is only −1.05 MW/m^3.

5.1.2. *Experimental results and predictions for coiled-tube heat exchanger*

Fig. 8 shows temporal profiles of pressure, hydrogen outflow rate and metal hydride and fluid temperatures measured during test 3C. The maximum hydrogen release rate in this test was set at 0.165 g/s and the fluid temperature at 27 °C. The vent valve was closed just after 8 min when the vessel pressure reached 7 bar. The lowest temperature of −40 °C was recorded by thermocouples T3c and T4c. The measured pressure profile and initial conditions were input to the model to obtain the plots shown in Fig. 9.

Fig. 9(a) shows the temporal profile of average metal hydride temperature along with spatial contour plots of the hydride temperature predicted by the model for test 3C. Two types of contour plots are shown. The circular contour plots represent a section of the computational domain normal to the central tube and halfway along the domain's width. The rectangular contour plots are for a section perpendicular to the circular section. Fig. 9(a) shows the metal hydride temperature decreases as the dehydriding reaction progresses. The average

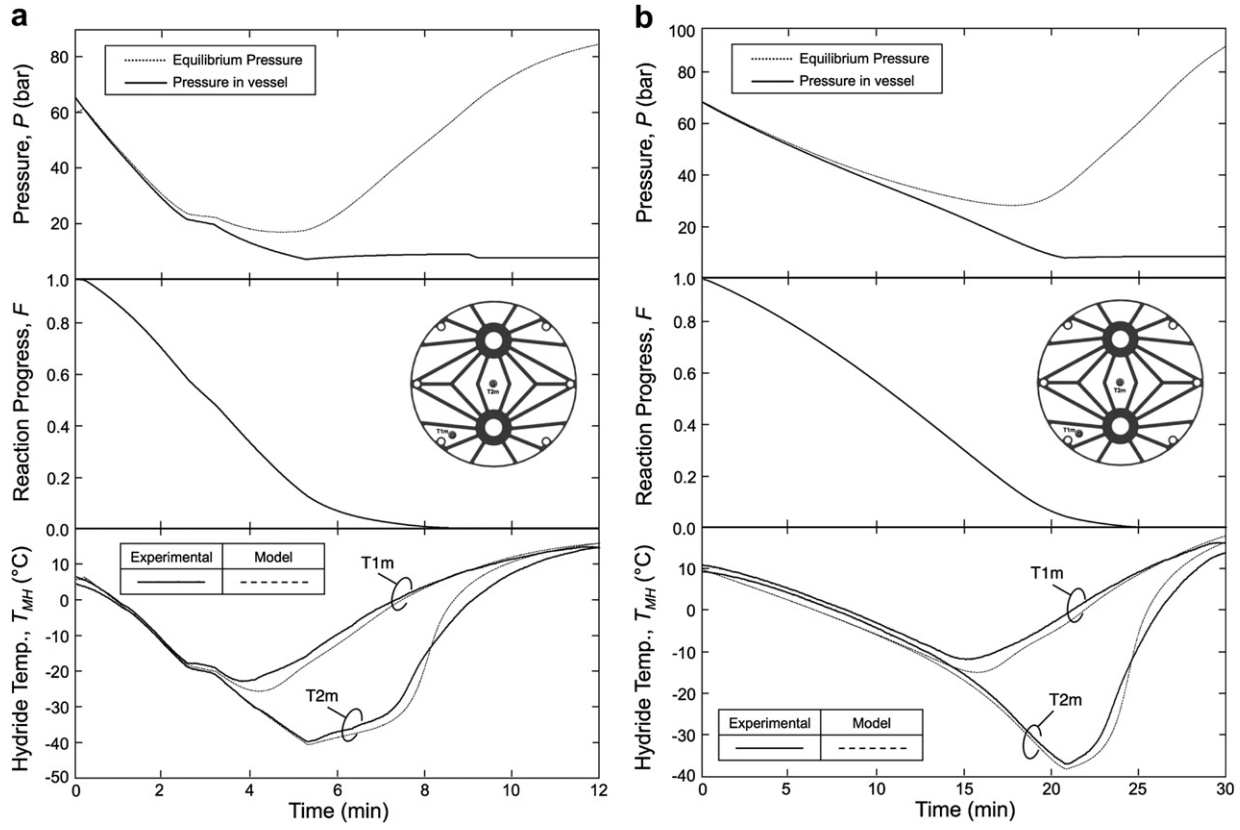

Fig. 10 – Comparison of model predictions of dehydriding reaction with experimental results for modular tube-fin heat exchanger for (a) test 1M and (b) test 2M.

hydride temperature reaches lowest value around 8.7 min, until which the contour plots show hydride temperatures are spatially fairly uniform. However, the contour plots show hydride particles reaching an even lower temperature of −40 °C at 10 min at thermocouple locations T3c and T4c, which is in agreement with both the magnitude and locations of the measured minimum temperature. Hydride particles farthest away from the fluid tube take to the longest to fully dehydride and reach their minimum temperature.

Fig. 9(b) shows a temporal profile of average reaction progress along with contour plots of the reaction progress. Within the first few minutes, hydride particles adjacent to the fluid tube are completely dehydrided. A sharp drop in reaction rate is observed at 8.5 min. This is because, at 8.5 min, the vent side on/off valve was closed to prevent the pressure from dropping further. Due to insufficient heat transfer initially, the hydride temperature remains low, causing the equilibrium pressure to remain low as well low. Hence, unless the hydride temperature increases or vessel pressure drops, the reaction will not increase. At 14 min, the particles are completely dehydrided everywhere except for a middle ring of hydride about halfway between the coil and central tube. At the end of 20 min, the metal hydride is on average 90% dehydrided.

Fig. 9(c) shows heat rate increases in magnitude from the onset of the reaction until 8.5 min, when the vent valve is closed. While the average heat rate reaches a peak value of −0.7 MW/m^3, peak rates as high as −3 MW/m^3 are achieved locally.

Figs. 8 and 9 demonstrate the effectiveness of the computational models, especially the contour plots, at capturing the detailed spatial and temporal variations of key heat exchanger performance parameters. This information can play a vital role in optimizing heat exchanger design, especially the placement of cooling surfaces within the hydride bed.

5.2. *Comparison of model predictions with experimental results for modular tube-fin heat exchanger*

Fig. 10(a) and (b) compare the model predictions for the modular tube-fin heat exchanger with experimental data from tests 1M and 2M, respectively. The average equilibrium pressure calculated from the model is plotted along with the vessel pressure measured during each test; the latter is provided as input to the model. The temperature-dependent equilibrium pressure decreases with decreasing metal hydride temperature during the dehydriding reaction. The dehydriding reaction occurs only when the vessel pressure is below the equilibrium pressure. In Fig. 10(a), for the first 2 min, the vessel pressure is almost equal to or just below the equilibrium pressure. As the reaction progresses further and the hydride temperature rises due to heat transfer from the warm fluid, the equilibrium pressure increases. During test 1M, the vent valve was closed at 2.6 min for a few seconds. This caused a decrease in dehydriding rate, which is captured by the model in the form of a change in slope of the dehydriding reaction

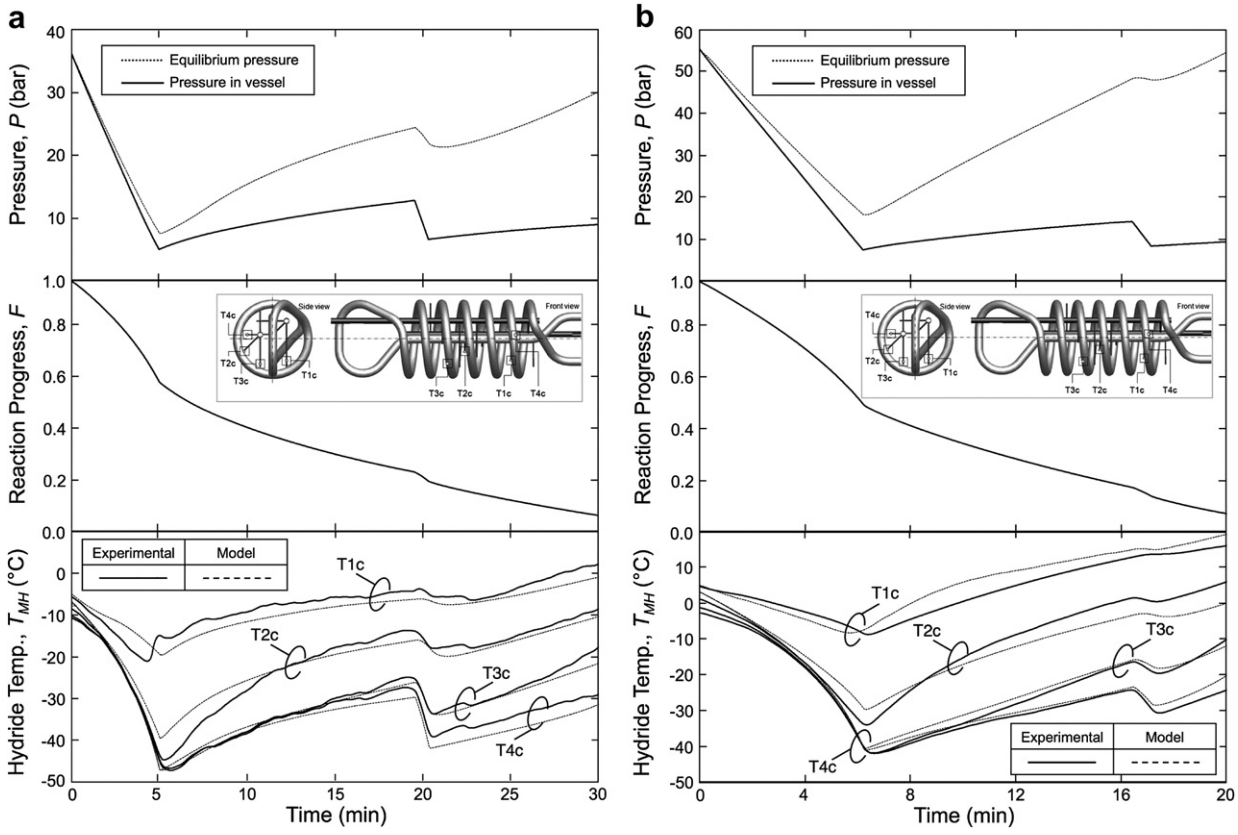

Fig. 11 – Comparison of model predictions of dehydriding reaction with experimental results for coiled-tube heat exchanger for (a) test 1C and (b) test 2C.

progress at 2.6 min. The reaction progress plotted in this figure is the volumetric average reaction progress predicted by the model. The nearing of completion of reaction is accompanied by increased metal hydride temperature due to reduced heat absorption rate. It can be observed from the plots of reaction progress and temperature that metal hydride temperature starts to rise once the powder is 80% dehydrided ($F = 0.2$). The predicted temperatures for locations T1m and T2m agree well with the thermocouple measurements for both tests. Slight disagreements between the predicted and measured temperatures toward the end of the reaction can be attributed to the use of constant thermal properties throughout the dehydriding reaction. Notice how the reaction is completed 15 min earlier in test 1M than in 2M because of the higher hydrogen outflow rate and higher pressure drop rate for test 1M.

5.3. *Comparison of model predictions with experimental results for coiled-tube heat exchanger*

Fig. 11(a) and (b) compare predictions of the 3-D coiled-tube heat exchanger model with experimental results from tests 1c and 2C, respectively. Notice how both figures capture the events of vent valve closing (to prevent the vessel pressure drop from dropping) in the form of slow changes in reaction progress. In test 1C, between 5 and 19 min, when the vent valve was closed, the metal hydride continued to dehydride and release hydrogen. The reaction progress dropped from 58% at 5 min to 23% at 19 min. This caused the vessel pressure to rise from 5 to 12.7 bar over the same period. Notice how the temperature increased every time the vent valve was closed and decreased when the valve was opened. This is captured remarkably well by the model in both trend and magnitude. Slight disagreements between the model predictions and measured temperatures can be attributed to (a) use of constant values of thermal properties in the model, (b) slight spatial variations in metal hydride density as the powder was being packed in the storage vessel around the coiled tube and thermocouples, and (c) slight shifting of thermocouple beads from intended locations during the packing process and as a result of expansion and contraction of the powder during the hydriding/dehydriding cycles. Compared to the modular tube-fin heat exchanger, the powder in the coiled-tube heat exchanger takes longer to dehydride due to inferior heat transfer rates.

6. Conclusions

This paper examined the dehydriding characteristics of the HPMH $Ti_{1.1}CrMn$, and provided a systematic approach to modeling these characteristics. The validity of this approach is verified by comparing model predictions with experimental results for two heat exchangers with drastically different designs: a modular tube-fin heat exchanger and a coiled-tube heat exchanger. Key findings from the study are as follows.

1. $Ti_{1.1}CrMn$ has excellent dehydriding properties and cold-start ability. It can dehydride and release hydrogen even at sub-zero temperatures. High hydrogen release rates can be achieved with an appropriately designed heat exchanger and the use of warm fluid (>20 °C). When used with a fuel cell, the heat generated by the fuel cell can be used to sustain the endothermic dehydriding reaction.
2. Dehydriding experiments were successfully performed with both the modular tube-fin heat exchanger and the coiled-tube heat exchanger. The heat exchanger occupies 29% of pressure vessel volume in the modular tube-fin heat exchanger storage system compared to 7% for the coiled tube. The former provided higher heat transfer rates compared to greater storage efficiency for the latter. The higher heat transfer rates enabled the modular tube-fin design to achieve faster hydrogen release and dehydriding rates. Under similar operating conditions, the coiled-tube design required 10–15 min longer to complete the dehydriding reaction.
3. 2-D and 3-D models were created in Fluent to assess the dehydriding performances of the modular tube-fin and coiled-tube heat exchangers, respectively. The models are quite accurate at predicting the spatial and temporal variations of metal hydride temperature during the dehydriding reaction.
4. Metal hydride particles located in warmer locations close to heat exchanger surfaces both begin and finish dehydriding earlier than particles farther away. The lowest temperature reached by the metal hydride decreases with increasing distance from the heat exchanger surfaces. Spatial variations in the dehydriding reaction cause heat desorption rate to reach values as high as 3.25 MW/m^3 in certain locations when the average rate is only 1 MW/m^3.
5. Dehydriding reaction rate can be accelerated by increasing heat exchanger fluid temperature and/or pressure drop rate. Hydrogen release rate can be made to match the fluctuating demands of an actual vehicle's fuel cell with the aid of a pressure regulator and/or by controlling the fluid temperature.

REFERENCES

[1] Takeichi N, Senoh H, Yokota T, Tsuruta H, Hamada K, Takeshita H, et al. Hybrid hydrogen storage vessel, a novel high pressure hydrogen storage vessel combined with hydrogen storage material. Int J Hydrogen Energy 2003;28:1121–9.
[2] Aceves SM, Berry GD, Martinez-Frias J, Espinosa-Loza F. Vehicular storage of hydrogen in insulated pressure vessels. Int J Hydrogen Energy 2006;31:2274–83.
[3] Aceves SM, Espinosa-Loza F, Ledesma-Orozco E, Ross TO, Weisberg AH, Brunner TC, et al. High-density automotive hydrogen storage with cryogenic capable pressure vessels. Int J Hydrogen Energy 2010;35:1219–26.
[4] Walker G. Solid-state hydrogen storage: materials and chemistry. Cambridge, England: Woodhead Publishing; 2008.
[5] Zuttel A. Materials for hydrogen storage. Mater Today 2003;6:24–33.
[6] Kaplan Y. Effect of design parameters on enhancement of hydrogen charging in metal hydride reactors. Int J Hydrogen Energy 2009;34:2288–94.
[7] Dhaou H, Souahlia A, Mellouli S, Askri F, Jemni A, Ben Nasrallah S. Experimental study of a metal hydride vessel based on a finned spiral heat exchanger. Int J Hydrogen Energy 2010;35:1674–80.

[8] Askri F, Ben Salah M, Jemni A, Ben Nasrallah A. Optimization of hydrogen storage in metal-hydride tanks. Int J Hydrogen Energy 2009;34:897–905.
[9] Pourpoint T, Velagapudi V, Mudawar I, Zheng Y, Fisher T. Active cooling of a metal hydride system for hydrogen storage. Int J Heat Mass Transfer 2010;53:1326–32.
[10] Visaria M, Mudawar I, Pourpoint T, Kumar S. Study of heat transfer and kinetics parameters influencing the design of heat exchangers for hydrogen storage in high-pressure metal hydrides. Int J Heat Mass Transfer 2010;53:2229–39.
[11] Mori D, Hirose K. Recent challenges of hydrogen storage technologies for fuel cell vehicles. Int J Hydrogen Energy 2009;34:4569–74.
[12] Poirier E, Dailly A. Thermodynamic study of the adsorbed hydrogen phase in Cu-based metal-organic frameworks at cryogenic temperatures. J Phys Chem 2008;112:13047–52.
[13] Visaria M, Mudawar I, Pourpoint T. Enhanced heat exchanger design for hydrogen storage using high-pressure metal hydride – part 2. Experimental results. Int J Heat Mass Transfer 2011;54:424–32.
[14] Jemni A, Ben Nasrallah S. Study of two-dimensional heat and mass transfer during desorption in a metal-hydrogen reactor. Int J Hydrogen Energy 1995;20:881–91.
[15] Dhaou JH, Mellouli S, Askri F, Jemni A, Ben Nasrallah S. Experimental and numerical study of discharge process of metal-hydrogen tank. Int J Hydrogen Energy 2007;32:1922–7.
[16] Muthukumar P, Maiya MP, Murthy SS. Experiments on a metal hydride based hydrogen compressor. Int J Hydrogen Energy 2005;30:879–92.
[17] Muthukumar P, Venkata Ramana S. Study of heat and mass transfer in $MmNi_{4.6}Al_{0.4}$ during desorption of hydrogen. Int J Hydrogen Energy 2010;35:10811–8.
[18] Mellouli S, Askri F, Dhaou H, Jemni A, Ben Nasrallah S. A novel design of a heat exchanger for a metal-hydrogen reactor. Int J Hydrogen Energy 2007;32:3501–7.
[19] Mellouli S, Askri F, Dhaou H, Jemni A, Ben Nasrallah S. Numerical study of heat exchanger effects on charge/discharge times of metal-hydrogen storage vessel. Int J Hydrogen Energy 2007;34:3005–17.
[20] Chung CA. Ci-Siang Lin. Prediction of hydrogen desorption performance of Mg_2Ni hydride reactors. Int J Hydrogen Energy 2009;34:9409–23.
[21] Chung CA, Ho Ci-Jyun. Thermal-fluid behavior of the hydriding and dehydriding processes in a metal hydride hydrogen storage canister. Int J Hydrogen Energy 2009;34:4351–64.
[22] Chaise A, de Rango P, Marty P, Fruchart D. Experimental and numerical study of a magnesium hydride tank. Int J Hydrogen Energy 2010;35:6311–22.
[23] Raju M, Ortmann JP, Kumar S. System simulation model for high-pressure metal hydride hydrogen storage systems. Int J Hydrogen Energy 2010;35:8742–54.
[24] Raju M, Kumar S. System simulation modeling and heat transfer in sodium alanate based hydrogen storage systems. Int J Hydrogen Energy 2011;36:1578–91.
[25] Tange M, Maeda T, Nakano A, Ito H, Kawakami Y, Masuda M, et al. Experimental study of hydrogen storage with reaction heat recovery using metal hydride in a totalized hydrogen energy utilization system. Int J Hydrogen Energy 2011;36:11767–76.
[26] Visaria M, Mudawar I, Pourpoint T. Enhanced heat exchanger design for hydrogen storage using high-pressure metal hydride – part 1. Design methodology and computational results. Int J Heat Mass Transfer 2011;54:413–23.
[27] Visaria M, Mudawar I. Coiled-tube heat exchanger for high-pressure metal hydride hydrogen storage systems – part 1. Experimental study. Int J Heat Mass Transfer 2011;55:1782–95.
[28] Visaria M, Mudawar I. Coiled-tube heat exchanger for high-pressure metal hydride hydrogen storage systems – part 2. Computational model. Int J Heat Mass Transfer 2011;55:1796–806.
[29] Mayer U, Groll M, Supper W. Heat and mass transfer in metal hydride reaction beds: experimental and theoretical results. J Less-Common Metals 1987;131:235–44.
[30] Suda S, Kobayashi N, Yoshida K. Reaction kinetics of metal hydrides and their mixtures. J Less Common Metals 1980;73:119–26.
[31] Voskuilen T, Zheng Y, Pourpoint T. Development of a Sievert apparatus for characterization of high pressure hydrogen sorption materials. Int J Hydrogen Energy 2010;35:10387–95.
[32] Flueckiger S, Voskuilen T, Pourpoint T, Fisher TS, Zheng Y. In situ characterization of metal hydride thermal transport properties. Int J Hydrogen Energy 2010;35:614–21.